RSC Applied Interfaces

ROYAL SOCIETY OF CHEMISTRY

PAPER

View Article Online
View Journal

Cite this: DOI: 10.1039/d5lf00356c

Electrocatalytic oxidation of methanol: role of thorium (Th) doping in $MoSe_2$

Pooja,[a] Sarita Yadav,[a] Ravinder Pawar *[a] and Rajeev Ahuja *[bc]

This study investigates the interaction of methanol (CH_3OH) with transition metal dichalcogenides (TMDCs), focusing particularly on the effect of thorium (Th) doping on the methanol oxidation reaction (MOR). Density functional theory (DFT) and periodic energy decomposition analyses reveal that Th doping enhances methanol adsorption through stronger orbital and electrostatic interactions, as supported by d-band center shifts and charge transfer analysis. Among various reaction pathways, methanol dehydrogenation *via* the CHOH* intermediate is identified as the most favorable due to its low Gibbs free energy. Electrochemical analyses show an onset potential of 1.02 V *vs.* RHE, a peak current density of 0.20 mA cm^{-2}, and remarkably low charge-transfer resistance, attributed to Th-induced electronic modulation. The calculated mass activity (M_A) of Th-doped $MoSe_2$ is 0.400 A mg^{-1}, surpassing several reported Pt-based catalysts, including Pt/gCN (0.310 A mg^{-1}) and Pt/NiCo-LDH (0.379 and 0.205 A mg^{-1}). CO stripping experiments and spectroscopic analyses (^{13}C NMR and FTIR) confirm complete CO oxidation. This work establishes Th-doped $MoSe_2$ as a robust and poison-resistant catalyst for sustainable energy applications, combining experimental validation with atomic-scale insights.

Received 13th November 2025,
Accepted 18th February 2026

DOI: 10.1039/d5lf00356c

rsc.li/RSCApplInter

Introduction

The electrocatalytic methanol oxidation reaction (MOR) has recently attracted significant attention owing to its abundant availability and ease of handling.[1–3] Compared to traditional water electrolysis, methanol oxidation presents a more cost-efficient alternative, positioning it as a viable alternative in the quest for sustainable energy solutions.[1–3] The effectiveness of this process depends primarily on the performance of catalysts, making methanol oxidation a key contributor to the green-alcohol economy and a promising pathway towards achieving a carbon-neutral future.[4,5] Platinum (Pt) is widely regarded as the most efficient metal catalyst for various electrocatalytic reactions, such as the hydrogen evolution reaction (HER), oxygen evolution reaction (OER), and oxygen reduction reaction (ORR).[6–8] High adsorption efficiency at nearly zero potential (*vs.* RHE) establishes it as a benchmark catalyst for these processes.[6–9] However, its use in the MOR is fraught with challenges. The high cost of Pt and its susceptibility to poisoning by the CO intermediate significantly hinder its practical application on a larger scale.[6–9] These intermediates block the active sites, impeding the adsorption of essential molecules and reducing catalytic efficiency.[6–9] Thus, the development of cost-effective catalysts with a higher density of active sites is imperative.[6–9]

Transition metal dichalcogenides (TMDCs) have emerged as promising substitutes due to their excellent physical properties, chemical stability, and high catalytic activity, all at a fraction of the cost of Pt.[10–15] Among these, the 2H phase of molybdenum diselenide ($MoSe_2$) stands out due to its superior electrical conductivity relative to molybdenum disulfide (MoS_2).[14–17] Regardless of its potential, the electrocatalytic performance of $MoSe_2$ is limited by its low density of active sites, which are predominantly confined to the unsaturated selenium (Se) edges.[14–17] This deficiency restricts its efficiency in high-performance MOR applications.[18] To address these limitations, rational design strategies are needed to optimize $MoSe_2$-based catalysts.

Enhancement in the catalytic performance can be achieved through two primary approaches: (i) increasing the number of active sites by doping other metals and (ii) integrating $MoSe_2$ with carbon-based materials to enhance conductivity and catalytic activity.[19–23] However, doping is a powerful strategy to tune the electronic and catalytic properties of $MoSe_2$.[24–26] By introducing dopants, $MoSe_2$ can be transformed into a more functional material, potentially surpassing the efficiency of Pt in electrolysis processes.[24–26] Metal doping, especially with rare-earth elements, holds promise in improving the catalytic properties of $MoSe_2$.[27–33]

[a] *Laboratory of Advanced Computation and Theory for Materials and Chemistry (LACTMC), Department of Chemistry, National Institute of Technology Warangal (NITW), Warangal, Telangana-506004, India. E-mail: ravinder_pawar@nitw.ac.in*
[b] *Condensed Matter Theory, Department of Physics and Astronomy, Uppsala University, Uppsala, 75120, Sweden. E-mail: rajeev.ahuja@physics.uu.se*
[c] *Department of Physics, Indian Institute of Technology Ropar, Punjab, India*

Doping introduces Se vacancies, thereby increasing the density of catalytically active sites. It also disrupts the coulombic balance, leading to atomic rearrangements and the emergence of new catalytic centers.[27–33] Additionally, such doping improves charge transfer kinetics, thereby accelerating the overall reaction rate.[27–33] Notwithstanding its potential, rare-earth doping for the MOR remains underexplored. Notably, thorium emerges as a compelling dopant due to its considerably lower market cost and higher natural abundance compared to Pt and traditional rare-earth elements,[27–33] presenting a viable and economical pathway for enhancing the electrocatalytic performance of $MoSe_2$.

Thorium (Th), the most abundant naturally occurring actinide, is increasingly recognized as a promising element for advanced energy and materials applications.[34–38] In recent years, its application landscape has expanded significantly including areas such as adsorption, radiation sensing, photocatalysis, and electrocatalysis.[37,39–42] Thorium possesses a long half-life ($\sim 1.4 \times 10^{10}$ years), resulting in low specific radioactivity and making it radiologically safer to handle compared to other actinides.[37] Its large ionic radius, strong oxophilicity, and the availability of 5f and 6d orbitals confer unique electronic and structural characteristics that can be advantageous in catalytic systems.[39–41] These features allow thorium-based materials to participate in a variety of chemical transformations with high thermal and chemical stability, particularly in harsh reaction environments.[39–42] As such, thorium-containing compounds are gaining attention as functional materials in fuel cells, redox catalysis, and other energy conversion systems.[39–42] Despite its numerous advantages, to the best of our knowledge, studies on Th-doped $MoSe_2$ remain scarce.

In this study, the methanol electrooxidation activity of thorium (Th)-doped $MoSe_2$ catalysts was investigated using a combined approach of density functional theory (DFT) simulations and experimental methods. Th-doped $MoSe_2$ catalysts were synthesized through a simple hydrothermal process. The structure and morphology of the synthesized catalysts were characterized using powder X-ray diffraction (PXRD), field emission scanning electron microscopy (FESEM), energy-dispersive X-ray spectroscopy (EDS), X-ray photoelectron spectroscopy (XPS), and high-resolution transmission electron microscopy (HR-TEM). To further elucidate the catalytic behavior, DFT calculations were employed to examine the structural and electronic properties of the Th-doped $MoSe_2$ catalyst, while cyclic voltammetry (CV) was used to assess its MOR activity. By integrating experimental results with theoretical models, this study provides a comprehensive analysis of the reaction mechanisms and pathways involved in the MOR on Th-doped $MoSe_2$. The results demonstrate that Th-doping significantly enhances the catalytic activity, enabling efficient and complete methanol oxidation. The increased active site density and improved electron transfer efficiency make Th-doped $MoSe_2$ a promising candidate for efficient and scalable MOR applications. Detailed synthetic processes, experimental methodology, and computational details are provided in the SI.

Computational details

To investigate the structure, stability, and electronic properties of the systems under consideration, spin-polarized DFT calculations were carried out using the Vienna *ab initio* simulation package (VASP).[43,44] The ion cores were represented using projector augmented wave (PAW) potentials.[45] The electron exchange and correlation energies were modelled using the Perdew–Burke–Ernzerhof (PBE)-sol[46] generalized gradient approximation (GGA).[47] A plane wave energy cutoff of 520 eV was utilized, with valence electron configurations for Mo: $5s^14d^5$, Se: $4s^24p^4$, and Th: $6d^27s^2$. Monkhorst–Pack[48] sampling was employed on the Brillouin zone, using a Γ-centered grid of 4 × 4 × 4. Geometry optimization was conducted until the energy variation reached below 10^{-6} eV, with forces acting on each atom below 0.003 eV Å^{-1}.

The change in Gibbs free energy (ΔG) for each reaction step was calculated using the Nørskov *et al.* method.[49] Under experimental conditions (U = 0, pH, pressure = 1 bar, temperature = 298 K), the free energy ΔG is calculated as follows:

$$\Delta G = \Delta E + \Delta \mathrm{ZPE} - T\Delta S + \Delta G_{\mathrm{U}} + \Delta G_{\mathrm{pH}}, \quad (1)$$

where ΔE is the reaction energy of the reactant and product adsorbed on the catalyst surface, derived from DFT analysis. The changes in zero-point energy (ΔZPE) and entropy (ΔS) for the reaction are also considered. ΔG_{pH} accounts for the pH correction, calculated as $\Delta G_{\mathrm{pH}} = -k_{\mathrm{b}}T\ln[\mathrm{H}^+] = 0.0593\mathrm{pH}$ when the pH is not zero.

The onset potentials were computed using the computational standard hydrogen electrode method, which accounts for the applied potential (U) by incorporating the term $\Delta G_{\mathrm{U}} = -eU$ to the free energy calculation for proton–electron pair formation. The electrochemical potential for each step was then determined as $\Delta U_{\mathrm{i}} = \Delta G_{\mathrm{i}}/e$, where ΔG_{i} represents the reaction free energy. Finally, the overall onset potential was estimated as $U_{\mathrm{onset}} = \max(\Delta G_{\mathrm{i}}/e)$, yielding the maximum value of the electrochemical potential.

Materials

Sodium molybdate (Na_2MoO_4, 99%), selenium powder (Se powder, 99%), thorium nitrate ($Th(NO_3)_4$, 99%), and hydrazine monohydrate ($H_4N_2{\cdot}H_2O$) were purchased from Sigma Aldrich. All the chemicals were used as received without further purification. Double-distilled (DI) water was obtained from ultrafiltration (Milli-Q, Millipore) units.

Synthesis of the Th–$MoSe_2$ catalyst

Th-doped $MoSe_2$ was synthesized *via* a typical hydrothermal method. Solution A was prepared by dissolving 0.484 g of Na_2MoO_4 in 50 mL of deionized (DI) water under continuous

stirring for 1 hour. Solution B was prepared by mixing 14 mL of $N_2H_4{\cdot}H_2O$ with 0.316 g of Se powder, followed by stirring at room temperature for 1 hour. Solution B was then added dropwise to solution A under constant stirring to obtain solution C. Solution D was prepared by dissolving 0.500 g of $Th(NO_3)_4$ in 100 mL of DI water. To maintain a low concentration of thorium, 3 mL of solution D was added dropwise to solution C under continuous stirring, and the mixture was stirred for an additional 1 hour. The resulting suspension was transferred to a 100 mL Teflon-lined stainless-steel autoclave and heated at 200 °C for 6 hours. A black precipitate was formed, which was collected by centrifugation and dried at 60 °C for 24 hours. The dried powder was then calcined at 350 °C for 1 hour to obtain the final Th-doped $MoSe_2$ product.

Electrochemical analysis

The MOR measurements were conducted using a MedPstat electrochemical analyzer equipped with a three-electrode system. An Ag/AgCl electrode served as the reference electrode, while a Pt electrode was employed as the counter electrode. The catalyst ink was prepared by dispersing 2.0 mg of catalyst in a mixture comprising 200 μL of isopropanol and 10 μL of Nafion (5%). Subsequently, the ink was ultrasonicated for 30 minutes to ensure a homogeneous dispersion of the catalyst. The resulting ink was then deposited onto the surface of a glassy carbon (GC) electrode with a diameter of 5 mm and air-dried. Liquid analyte analysis was carried out using ^{1}H-NMR on a Bruker Avance-III 400 MHz NMR spectrometer, with $CDCl_3$ as the solvent.

Results and discussion

Interaction of CH_3OH with transition metal dichalcogenides

Systematic DFT calculations were performed to investigate the adsorption properties of the TMDCs, considering MoS_2, $MoSe_2$, Th-doped MoS_2, and Th-doped $MoSe_2$. A 4 × 4 super cell is used in the present investigation for all the considered TMDCs. The optimized geometries of this structure and their interaction with methanol are illustrated in Fig. 1(a). Notably, the adsorption behavior of methanol varies with the nature of the TMDCs. The calculated distances between the methanol molecule and the nearest surface atoms were 3.28 Å (MoS_2), 3.13 Å ($MoSe_2$), 3.29 Å (Th-doped MoS_2), and 3.11 Å (Th-doped $MoSe_2$), respectively.

To gain deeper insight into the nature of methanol–catalyst interactions, periodic energy decomposition analysis (PEDA)[50,51] was performed using the Amsterdam density functional (ADF)[52] as shown in Fig. 1(b). The computational methodology of PEDA is detailed in the SI. All calculations were carried out using the GGA-PBEsol exchange–correlation functional with a Slater-type DZP basis set.[53] The PEDA results indicate that methanol exhibits the strongest interaction with the Th-doped $MoSe_2$ catalyst, with an interaction energy of −3.54 kcal mol^{-1}. In contrast, comparatively weaker interactions were observed for the other TMDCs considered in the present investigation, *i.e.*, $MoSe_2$ (−2.15 kcal mol^{-1}), MoS_2 (−2.34 kcal mol^{-1}), and Th-doped MoS_2 (−2.21 kcal mol^{-1}). In the CH_3OH–Th-doped $MoSe_2$ catalyst, the repulsive interaction component was Pauli repulsion (4.14 kcal mol^{-1}), counterbalanced by substantial electrostatic (−2.76 kcal mol^{-1}) and orbital (−4.91 kcal mol^{-1}) contributions. The orbital interaction is the dominant interaction between the methanol and Th-doped $MoSe_2$ catalyst. For the other TMDCs, the orbital interactions were considerably smaller (−2.85, −2.90, and −3.01 kcal mol^{-1} for $MoSe_2$, MoS_2, and Th-doped MoS_2, respectively) than that for Th-doped $MoSe_2$. The dominant interaction is Pauli repulsion between the methanol and TMDCs, namely $MoSe_2$ (3.47 kcal mol^{-1}), MoS_2 (2.87 kcal mol^{-1}), and Th-doped MoS_2 (3.37 kcal mol^{-1}), respectively. Furthermore, the calculated electrostatic components for $MoSe_2$ (−3.04 kcal mol^{-1}), MoS_2 (−2.32 kcal mol^{-1}), and Th-doped MoS_2 (−2.47 kcal mol^{-1}), respectively. Notably, the interaction within the methanol

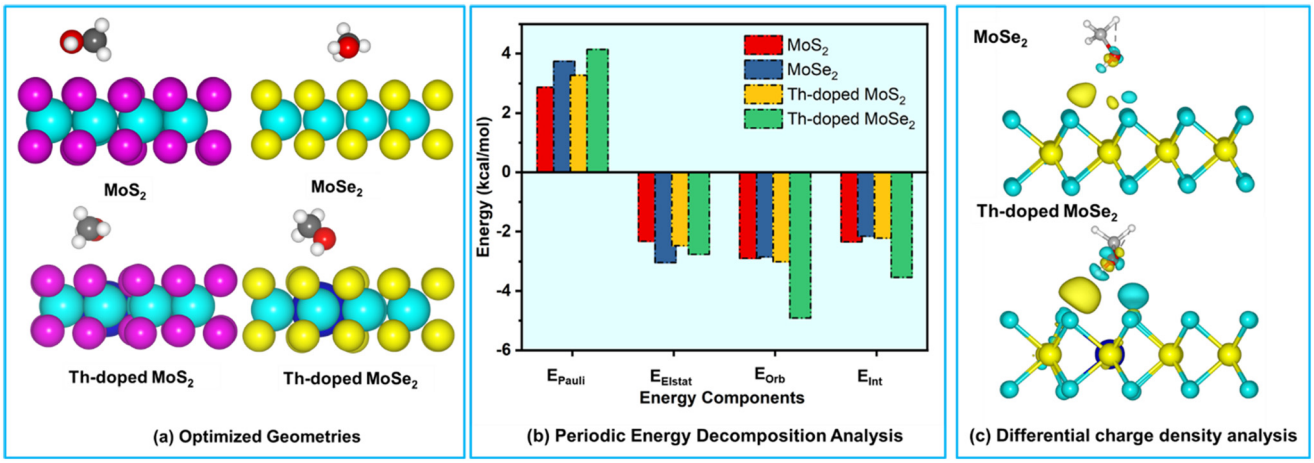

Fig. 1 (a) Optimized geometry of methanol–TMDCs, (b) periodic energy decomposition analysis of methanol–TMDCs, TMDCs are MoS_2, $MoSe_2$, Th-doped MoS_2, and Th-doped $MoSe_2$, and (c) differential charge density analysis of pristine $MoSe_2$ and Th-doped $MoSe_2$ with methanol (isosurface value = 0.008 a.u.). Color code: cyan: Mo, pink: S, yellow: Se, blue: Th, gray: C, white: H, and red: O.

and Th-doped $MoSe_2$ was dominated by attractive electrostatic and orbital contributions, indicating significant charge redistribution and strong orbital overlapping. These findings highlight that methanol adsorption on the Th-doped $MoSe_2$ surface induces substantial electronic rearrangement, which promotes methanol activation and subsequent oxidation.

To elucidate the role of the Th atom in methanol adsorption, differential charge density analyses ($p(C_{Th-MoSe_2/MoSe_2-intermediate})$ – p(intermediate) – $p(CX_{Th-MoSe_2/MoSe_2})$) were performed and compared with undoped $MoSe_2$ as shown in Fig. 1(c). The results show a significant increase in localized charge density at the methanol–Th-doped $MoSe_2$ interface, indicating stronger interactions compared to the pristine $MoSe_2$ surface. This charge redistribution reveals that the Se atom adjacent to Th strongly interacts with the active site of CH_3OH. The notable orbital interactions arising from substantial charge redistribution during methanol adsorption on Th-doped $MoSe_2$ further confirm its promising activation of the methanol molecule. Overall, the PEDA and differential charge density analysis show that Th-doped $MoSe_2$ is the most promising catalyst, offering favorable energetics for methanol adsorption and dissociation into key MOR intermediates.

Electronic properties

Furthermore, to probe the electrocatalytic behaviour of Th-doped $MoSe_2$ catalysts, an in-depth analysis of their electronic properties was conducted. The spin-polarized projected density of states (PDOS) is illustrated in Fig. 2.

The valence band is primarily composed of Se 4p states, with its uppermost portion dominated by Mo d_{z^2} and $d_{x^2-y^2}$ orbitals. In contrast, the conduction band is formed by unoccupied Mo 4d states, as shown in Fig. 3. Upon doping $MoSe_2$ with a Th atom, significant alterations in the electronic distribution are observed. The introduction of the Th atom reduces the intrinsic band gap of $MoSe_2$ and generates new electronic states within the Fermi level.

The wavefunctions associated with the lowest unoccupied crystal orbitals (LUCOs) and the highest occupied crystal orbitals (HOCOs) are primarily localized around the Mo and Se atoms, respectively, as confirmed by the PDOS analysis. Th-doping alters the electronic distribution, localizing the electroactive regions around the Se sites near the dopant. This modification results in a significant contribution from the Se 4p orbitals to the LUCO, particularly for Se atoms adjacent to the Th impurity, which act as optimal anchoring sites for the MOR. Furthermore, the enhanced electronic conductivity arises from the synergistic interaction between the Mo and Se atoms at the Fermi level, which reduces charge transfer resistance. Th-doping also imparts metallic properties to $MoSe_2$, promoting efficient electron movement from the valence band to the conduction band. The presence of electron density at the Fermi level further supports efficient electron transfer during the reaction, as corroborated by PEDA and charge transfer analysis. Overall, the metallic characteristics of Th-doped $MoSe_2$ result in the lowest charge-transfer resistance and the highest electronic conductivity, thereby significantly enhancing MOR efficiency.

The d-band center theory, introduced by Hammer and Nørskov,[54] provides a quantitative framework to relate the electronic structure of transition metal catalysts to their adsorption properties and catalytic behavior. In this model, the relative position of the d-band center (ε_d) with respect to the Fermi level (E_F) governs the strength of metal–adsorbate interactions.[55,56] When a molecule interacts with a catalyst, the adsorption capacity is largely governed by the position of the d-orbital center of the metal atoms.[57] Hence, the d-band center theory provides a valuable framework for explaining the interplay between the electronic structure and adsorption energy, thereby rationalizing the coordination ability and electrocatalytic performance of catalysts from the perspective of orbital energetics.[58,59] When the d-band center lies closer to E_F, the overlap between metal d-states and the molecular orbitals of the adsorbate increases, resulting in stronger adsorption due to stabilization of bonding orbitals and reduced filling of antibonding states.[55,56] Conversely, a downward shift of the d-band center weakens adsorption because antibonding orbitals become more populated.[55,56] To evaluate these effects in the present work, we systematically compared the electronic structure and

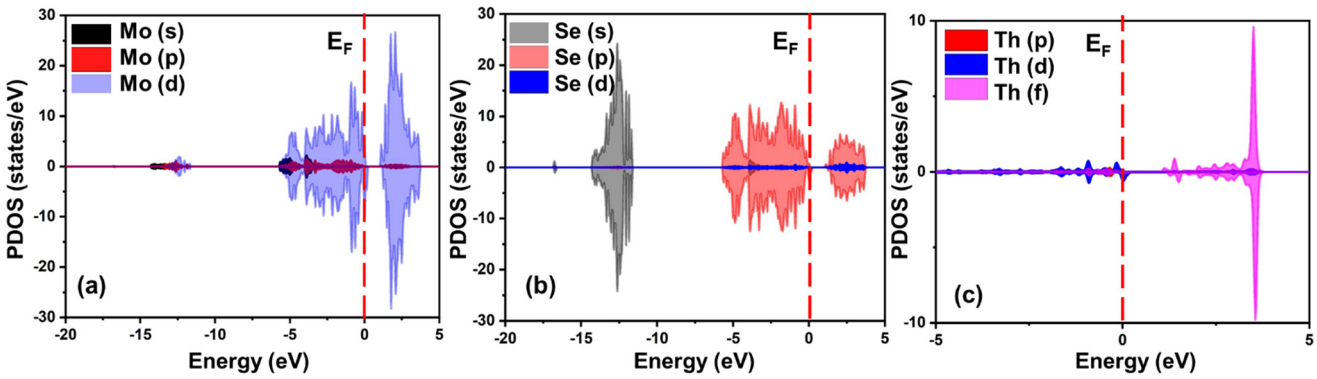

Fig. 2 Calculated projected density of states of (a) Mo, (b) Se, and (c) Th of Th-doped $MoSe_2$.

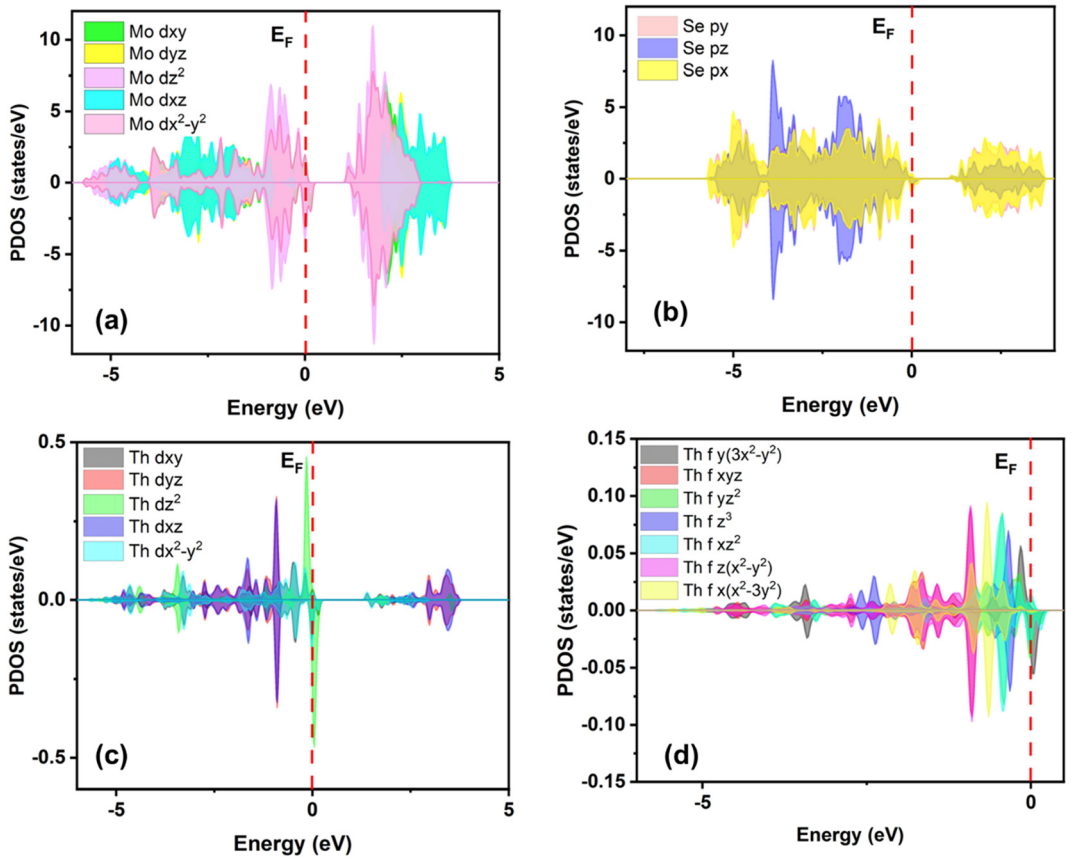

Fig. 3 Calculated projected density of states of (a) Mo-d, (b) Se-p, (c) Th-d, and (d) Th-f orbitals.

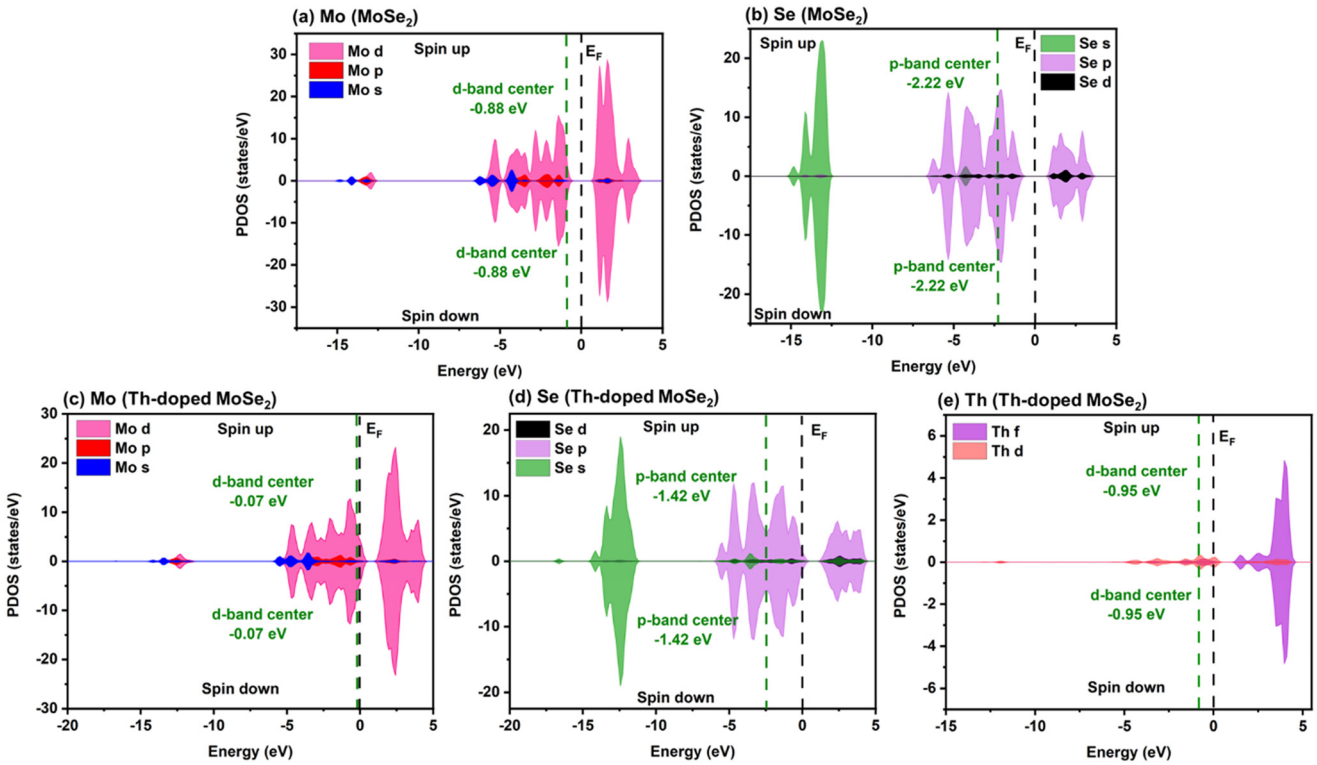

Fig. 4 Calculated projected density of states and d-band centers of pristine $MoSe_2$ and Th-doped $MoSe_2$ after the adsorption of CH_3OH.

adsorption characteristics of pristine $MoSe_2$ with those of Th-doped $MoSe_2$ upon CH_3OH adsorption, as shown in Fig. 4.

For pristine $MoSe_2$ upon CH_3OH adsorption, the d-band center of Mo is located at −0.88 eV, while the p-band center of Se lies deeper at −2.22 eV. The relatively higher energy of Mo indicates moderate adsorption, whereas Se contributes its p-states to stabilize adsorbates. In contrast, Th doping significantly modifies the electronic structure. For CH_3OH-adsorbed Th–$MoSe_2$, the Mo d-band shifts upward to −0.07 eV, and the Se p-band shifts to −1.47 eV. This upward shift brings the electronic states closer to the Fermi level, enhancing orbital overlap with CH_3OH molecular orbitals. As a result, bonding states are stabilized while antibonding states remain less populated, strengthening adsorption and facilitating CH_3OH activation.

Furthermore, the d-band centers of Mo and Th differ substantially, with Th exhibiting higher energy states in both spin channels. This energy mismatch promotes electron transfer from Mo to Th, while Se, with its more negative band center, acts as an electron reservoir. The synergistic interactions among Mo, Th, and Se thus optimize charge redistribution, stabilize adsorbed intermediates, and enhance the catalytic efficiency toward methanol oxidation. In addition, the shift of the Se p-band center in Th-doped $MoSe_2$ altered the donor–acceptor characteristics of the catalyst surface, enabling Se atoms to participate more effectively in electron exchange and thereby enhancing overall electron transfer. Importantly, the upward shift of the Mo d-band center in the Th-doped system brings it closer to the Fermi level, which stabilizes the bonding orbitals while keeping the antibonding states less occupied. This electronic configuration enhances the interaction with CH_3OH, resulting in stronger adsorption and more efficient activation of the methanol molecule compared with pristine $MoSe_2$. Upon CH_3OH adsorption, the enhanced orbital overlap between the molecular orbitals and the unoccupied d-states of the catalyst increases the adsorption energy, thereby facilitating bond activation and promoting the transformation of the methanol substrate through stable adsorption–desorption cycles. The band structure of Th-doped $MoSe_2$ is provided in the SI, Fig. S1.

Based on these observations, the mechanistic discussion focuses on Th-doped $MoSe_2$, as its modified electronic structure enables stronger CH_3OH adsorption and improved activation compared with pristine $MoSe_2$.

Mechanistic insights into catalytic behaviour

Based on the above discussion, Th-doped $MoSe_2$ has emerged as a promising catalyst for the MOR. The adsorption of intermediates during the electrochemical oxidation of methanol was systematically examined to elucidate the underlying mechanism. Methanol dehydrogenation into CO and H_2 on the Th-doped $MoSe_2$ surface proceeds *via* four distinct pathways, summarized as follows:

$$CH_3OH^* \rightarrow CH_3O^* + H^* \rightarrow CH_2O^* + H^* \rightarrow CHO^* + H^* \rightarrow CO^* + H^* \text{ (Scheme 1)} \quad (2)$$

$$CH_3OH^* \rightarrow CH_2OH^* + H^* \rightarrow CH_2O^* + H^* \rightarrow CHO^* + H^* \rightarrow CO^* + H^* \text{ (Scheme 2)} \quad (3)$$

$$CH_3OH^* \rightarrow CH_2OH^* + H^* \rightarrow CHOH^* + H^* \rightarrow CHO^* + H^* \rightarrow CO^* + H^* \text{ (Scheme 3)} \quad (4)$$

$$CH_3OH^* \rightarrow CH_2OH^* + H^* \rightarrow CHOH^* + H^* \rightarrow COH^* + H^* \rightarrow CO^* + H^* \text{ (Scheme 4)} \quad (5)$$

These pathways can be broadly categorized into two types: (i) initiate with O–H bond cleavage (Scheme 1) and (ii) pathways involving initial C–H bond cleavage (Schemes 2–4). The different intermediates generated during CH_3OH dissociation are illustrated in Fig. 5.

Activation of the O–H bond (Scheme 1)

The cleavage of the O–H bond in methanol begins with the removal of a hydrogen atom from the hydroxyl group, producing CH_3O^* and H*. Methanol initially adsorbs on the Th-doped $MoSe_2$ surface with the hydroxyl hydrogen oriented towards a Se site, leading to the initiation of oxidation. Subsequent dehydrogenation produces CH_2O^*, with the hydrogen atom migrating to a nearby Se atom (adjacent to the Th atom). The process continues with CH_2O adsorption and further dehydrogenation to CHO*, leading to CO formation, as shown in Fig. 6(a).

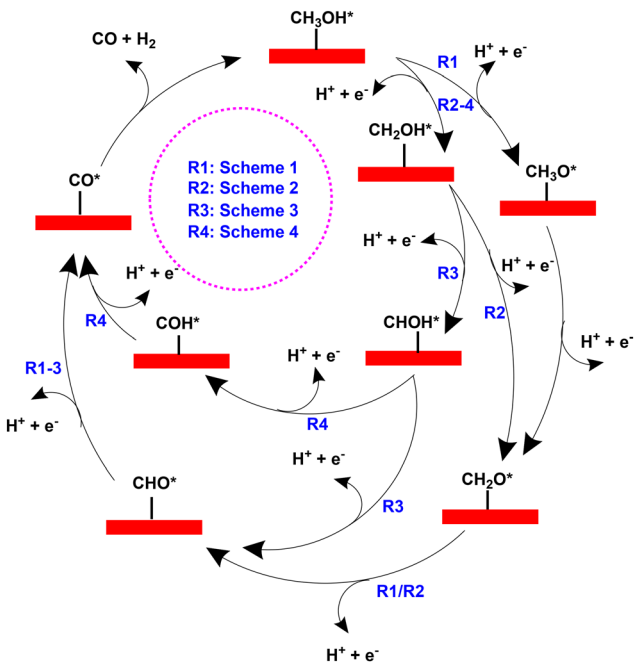

Fig. 5 Schematic representation of the reaction mechanism.

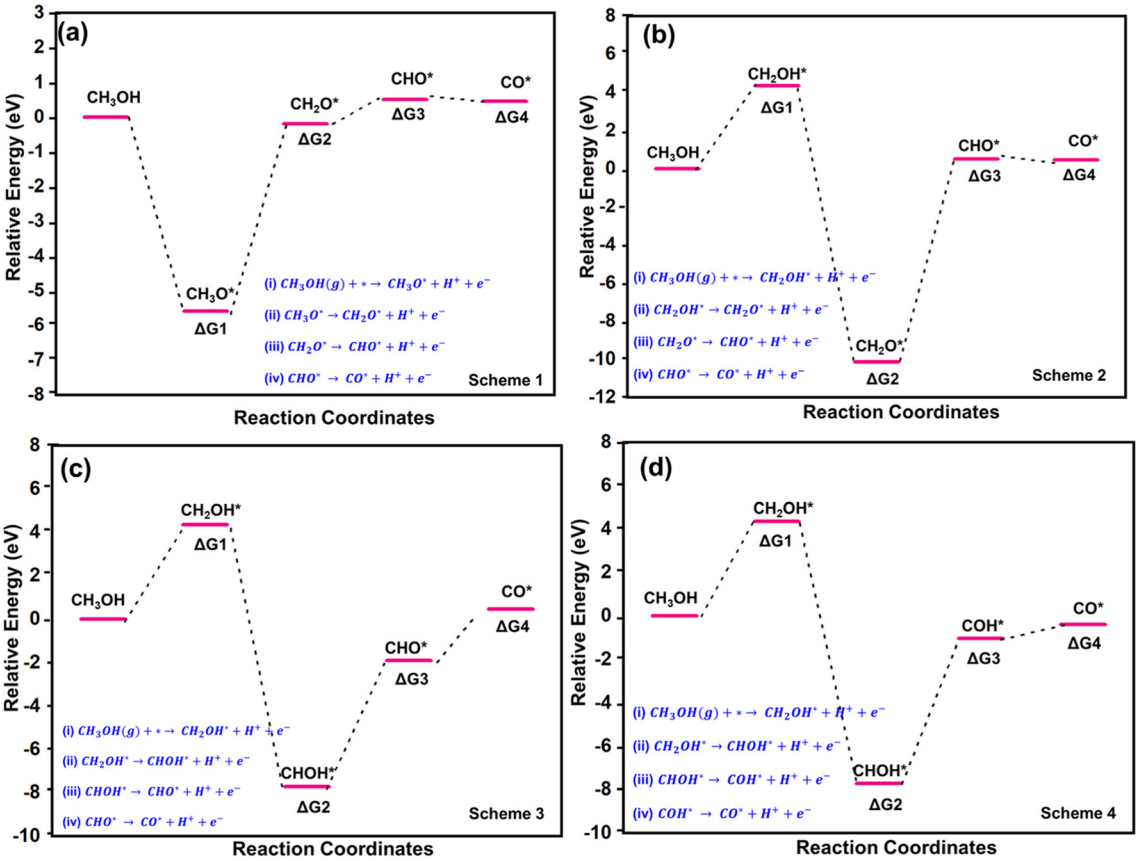

Fig. 6 Relative Gibbs free energy diagram for the MOR using different mechanistic schemes: (a) Scheme 1, (b) Scheme 2, (c) Scheme 3, and (d) Scheme 4. The * represents the adsorbed intermediate on the active surface of the Th-doped $MoSe_2$ catalyst.

Activation of the C–H bond (Schemes 2–4)

Pathways that begin with C–H bond activation differ from Scheme 1, starting with CH_3OH dehydrogenation to CH_2OH*. The intermediate adsorbs on the Th-doped $MoSe_2$ surface through a C–Se bond. Further dehydrogenation can proceed *via* O–H bond cleavage to yield CH_2O (Scheme 2) or C–H bond cleavage to produce CHOH (Scheme 3), as illustrated in Fig. 6(b and c). The final step involves the conversion of CHO* to CO* and H*, where CO adsorbs onto the surface through a C–Se bond, facilitating efficient hydrogen transfer. In Scheme 4, CHOH undergoes additional dehydrogenation to form COH, which subsequently converts to CO, as shown in Fig. 6(d). This pathway features enhanced CO adsorption stability due to a stronger C–Se bond (1.42 Å).

Table 1 Calculated relative Gibbs free energy (ΔG, in eV) along with various reaction pathways

Reaction path	Relative Gibbs free energy			
	$\Delta G1$	$\Delta G2$	$\Delta G3$	$\Delta G4$
Scheme 1	−5.58	−0.188	0.50	0.45
Scheme 2	4.35	−10.13	0.50	0.45
Scheme 3	4.35	−7.72	−1.89	0.45
Scheme 4	4.35	−7.72	−1.05	−0.39

The electron density distribution around Se sites adjacent to the Th dopant plays a crucial role in stabilizing intermediates, further improving catalytic efficiency. These mechanistic insights provide a deeper understanding of the catalytic behaviour of Th-doped $MoSe_2$, demonstrating its potential for efficient methanol electrooxidation through optimized reaction pathways and stable adsorption configurations. The calculated relative Gibbs free energies are displayed in Table 1.

Mechanistic insights and comparison of reaction pathways

The influence of Th-doping on the electronic environment also prevents over binding of dissociated hydrogen on the catalyst surface, thereby enhancing catalytic efficiency. The Th-doped $MoSe_2$ exhibits robust adsorption and efficient electron transfer between methanol and the catalyst surface, particularly during the initial adsorption of CH_3OH. The overlap of electronic states supports efficient charge transfer, contributing to the stability of the catalyst. The elementary steps of the MOR involving electron transfer and charge transfer, and their corresponding reaction free energy expressions are provided in the SI (Fig. S2 and S3, and Table S1). The calculated total density of states for various reaction intermediates and the corresponding elementary reactions

involved in methanol dehydrogenation are detailed in the SI (Fig. S3). The mechanistic pathways highlight that the dissociation of the O–H bond (Scheme 1) forms a stable CH_3O* intermediate (ΔG = −5.58 eV) on the Th-doped $MoSe_2$ surface and makes it more challenging for further dissociation of hydrogen to form a CH_2O* intermediate. Thus, Scheme 1 is less favourable, leaving Schemes 2–4 as viable pathways for methanol dehydrogenation.

Upon C–H bond cleavage, CH_3OH initially dehydrogenates to form CH_2OH, which can follow two distinct routes, *i.e.*, Scheme 2: $CH_2OH \rightarrow CH_2O \rightarrow CHO$ and Scheme 3: $CH_2OH \rightarrow CHOH \rightarrow CHO$. Both pathways ultimately converge to CHO formation as the final intermediate before CO is released. Notably, the dehydrogenation route *via* CHOH (with a Gibbs free energy ΔG = −1.89 eV) is thermodynamically more favourable compared to the CH_2O pathway (ΔG = 0.50 eV), due to the weaker adsorption of CH_2O, which limits catalytic efficiency. Therefore, Scheme 3 emerges as the most efficient pathway among the feasible routes. The fourth pathway involves the conversion of CHOH to COH, which further dehydrogenates to produce CO. However, the formation of CO from COH is characterized by stable adsorption with a Gibbs free energy ΔG of −0.388 eV, making it less favourable for an efficient MOR. The Gibbs free energy of CO in Scheme 3 (ΔG = 0.45 eV) suggests enhanced anti-poisoning activity, preventing the catalyst surface from being blocked by CO adsorption. Therefore, the CO anti-poisoning effect was also scrutinized and provided in the subsequent section.

Synthesis of Th-doped $MoSe_2$

Th-doped $MoSe_2$ nanostructures were synthesized *via* a simple hydrothermal method using standard precursors, namely sodium molybdate, selenium powder, thorium nitrate hydrate, and hydrazine monohydrate. The resulting Th-doped $MoSe_2$ nanosheets exhibited a loosely packed morphology, as

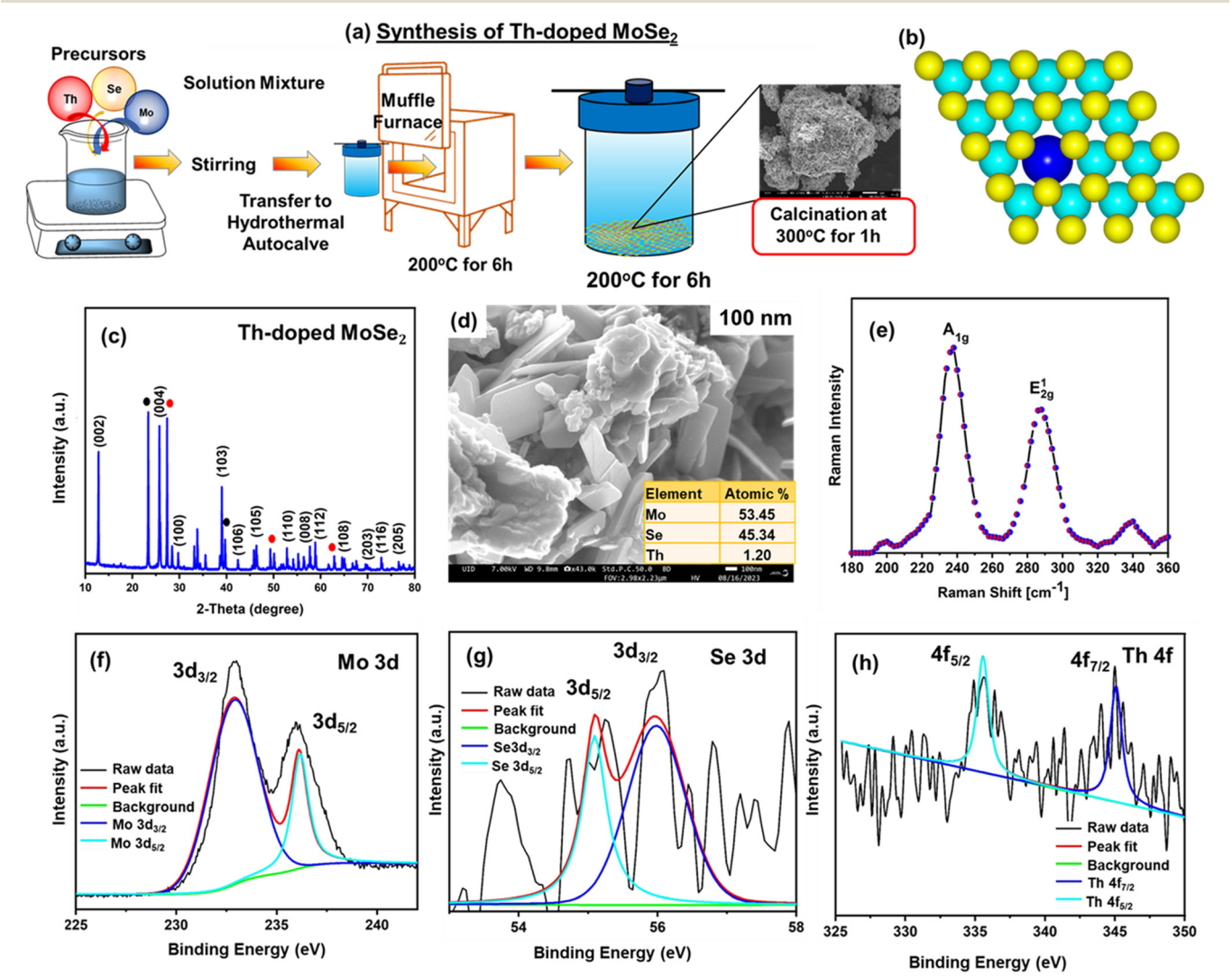

Fig. 7 (a) Schematic representation of the preparation of Th-doped $MoSe_2$ *via* a hydrothermal method, (b) supercell of the considered Th-doped $MoSe_2$, (c) XRD pattern of Th-doped $MoSe_2$, (d) FESEM image, (e) Raman spectrum of Th-doped $MoSe_2$, (f) XPS spectrum of Mo, (g) XPS spectrum of Se, and (h) XPS spectrum of Th. Color code: cyan: Mo, yellow: Se, and blue: Th.

shown in Fig. 7(a). A schematic representation of the supercell structure is provided in Fig. 7(b). The diffraction pattern of Th-doped $MoSe_2$ displayed similar characteristic peaks to those of pristine $MoSe_2$, confirming that Th incorporation does not alter the intrinsic hexagonal crystal structure (SI, Fig. S4(a)). The lattice parameters obtained from the XRD patterns of the Th-doped 2H-$MoSe_2$ phase were calculated to be a = 3.29 Å and c = 12.92 Å, with a c/a ratio of 3.92 (Fig. 7(c)). These values are in close agreement with the reference hexagonal $MoSe_2$ structure (ICDD card no. 29–0914: $P6_3/mmc$, a = 3.30 Å, c = 12.97 Å, c/a = 3.93). A slight decrease in the c lattice constant and c/a ratio upon Th doping suggests substitutional incorporation of Th at the Mo sites rather than interstitial doping.[60,61] Furthermore, no secondary phases were detected in the XRD patterns, supporting the conclusion that Th atoms are incorporated into the $MoSe_2$ lattice without significant peak shifts. Although the exact lattice position of Th cannot be conclusively determined, a comparison of ionic radii suggests that substitution at the Mo site is more plausible than at the Se site. The ionic radius of Th^{4+} (237 pm) is relatively close to that of Mo^{4+} (209 pm), with a difference of 28 pm, whereas the size mismatch between Th^{4+} and Se^{2-} (109 pm) is much larger (128 pm), making substitution at the Se site energetically less favorable and more likely to induce lattice distortion. This strongly supports the likelihood of Th substituting Mo sites while preserving the overall lattice symmetry. Similar observations have been reported in the literature for other heavy-metal substitutions at Mo sites in $MoSe_2$.[62–64]

Further morphological analysis was conducted using FESEM, as shown in Fig. 7(d). The FESEM images reveal that the Th-doped $MoSe_2$ nanosheets possess a dense microstructure, with well-defined grains approximately 100 nm in size. The captured images also indicate the formation of thin, loosely aggregated nanosheets, consistent with the nanoscale crystallinity observed in the XRD analysis. Additionally, Energy Dispersive Spectroscopy (EDS), illustrated in the SI (Fig. S4(b)), confirms the presence and atomic ratios of Th-doped $MoSe_2$ ($MoSe_{0.85}Th_{0.02}$), verifying the heterogeneous composition of the synthesized material.

The Raman spectrum of Th-doped $MoSe_2$ is schematically illustrated in Fig. 7(e). The Th-doped sample investigated in this study was identified as a 2H polytype based on the analysis of its low-frequency Raman spectra.[65,66] In pristine monolayer $MoSe_2$, the A_{1g} and $E_{2g}{}^1$ modes appear at 240.4 cm^{-1} and 286.8 cm^{-1}, respectively. In the Raman spectra of Th-doped $MoSe_2$, the corresponding modes were observed at 238 cm^{-1} (A_{1g}) and 286 cm^{-1} ($E_{2g}{}^1$). The E_{1g} mode, typically located near 169 cm^{-1}, is forbidden in backscattering geometry, while the A_{2u} mode, appearing at around 343 cm^{-1}, is Raman inactive; however, the latter can emerge under specific excitation conditions due to resonance effects.[65–67] Notably, the A_{1g} mode is particularly sensitive to doping, and the observed redshift is attributed to phonon softening induced by Th substitution. This softening arises from the increased atomic mass of Th and the local lattice distortions introduced into the $MoSe_2$ matrix. Similar shifts of the A_{1g} mode have been reported in the literature for other heavy-metal substitutions at Mo sites in $MoSe_2$.[60,64,65]

To investigate the chemical composition, the XPS analysis was performed. The XPS spectra confirm the presence of Mo, Se, and Th as key constituents, as shown in Fig. 7(f–h). Peaks corresponding to Mo $3d_{3/2}$ and Mo $3d_{5/2}$ orbitals, located at 235.59 and 232.45 eV, respectively, indicate that Mo is present in its Mo(IV) oxidation state. Similarly, the Se 3d orbitals, with peaks at 54.70 and 55.50 eV, corresponding to Se $3d_{5/2}$ and $3d_{3/2}$, confirm Se in its Se(II) oxidation state. The Th 4f orbitals, with peaks at 344.98 and 335.67 eV for Th $4f_{5/2}$ and Th $4f_{7/2}$, confirm the presence of Th in its Th(IV) state. XPS analysis confirms the presence of Mo^{4+}, Se^{2-}, and Th^{4+} through characteristic binding energies. The Th^{4+} oxidation state, like that of Mo^{4+}, along with the unchanged Se 3d peak positions, suggests that thorium likely substitutes Mo atoms in the $MoSe_2$ lattice. This is further supported by the marginal distortions in the Se peaks, indicating minimal interaction of Th with Se sites. These findings suggest the formation of a Se–Th–Se layered structure within the $MoSe_2$ matrix, as shown in Fig. 7(f–h) and the SI (Fig. S4(c)).

The structure of Th-doped $MoSe_2$ was also characterized using HR-TEM. A sample of Th-doped $MoSe_2$ was prepared and analyzed on a TEM grid. Fig. 8(a–c) reveal a homogeneous, well-structured Th-doped $MoSe_2$ sample exhibiting a continuous 2H phase. Experimental and computational evidence from the literature suggests that the H-stacking configuration of few-layer $MoSe_2$ follows an AB_1 stacking pattern.[68,69] Each layer of $MoSe_2$ consists of one layer of hexagonally arranged Mo atoms covalently bonded to two atomic layers of Se atoms on either side of the plane.[70] The HR-TEM images, shown in Fig. 8(a) and (b), clearly depict the layered structure of the material. The inset in Fig. 8(c) confirms an interlayer spacing of 0.65 nm, consistent with the (002) plane of 2H-$MoSe_2$.[71] Additionally, lattice spacings of 0.28 nm and 0.16 nm, corresponding to the (100) and (110) planes, were identified, aligning well with theoretical calculations of the in-plane lattice constant for $MoSe_2$.[68–71] The HR-TEM analysis demonstrates the continuous and high-quality of the synthesized films, although some wrinkles are visible at the edges of the film, as shown in Fig. 8(c), attributed to mechanical scratching during TEM sample preparation. Fig. 8(d) presents a selected area electron diffraction (SAED) pattern, acquired with an aperture size of ~5 nm, which indicates the polycrystalline nature of the synthesized catalyst. Furthermore, high-angle annular dark field (HAADF) scanning and EDS elemental mapping confirm the homogeneous distribution of Mo, Se, and Th within the catalyst matrix, validating the incorporation of all elements into the material, as shown in Fig. 8(e–i). The HR-TEM analysis is consistent with the XRD patterns, further confirming the structural and compositional integrity of the Th-doped $MoSe_2$ catalyst.

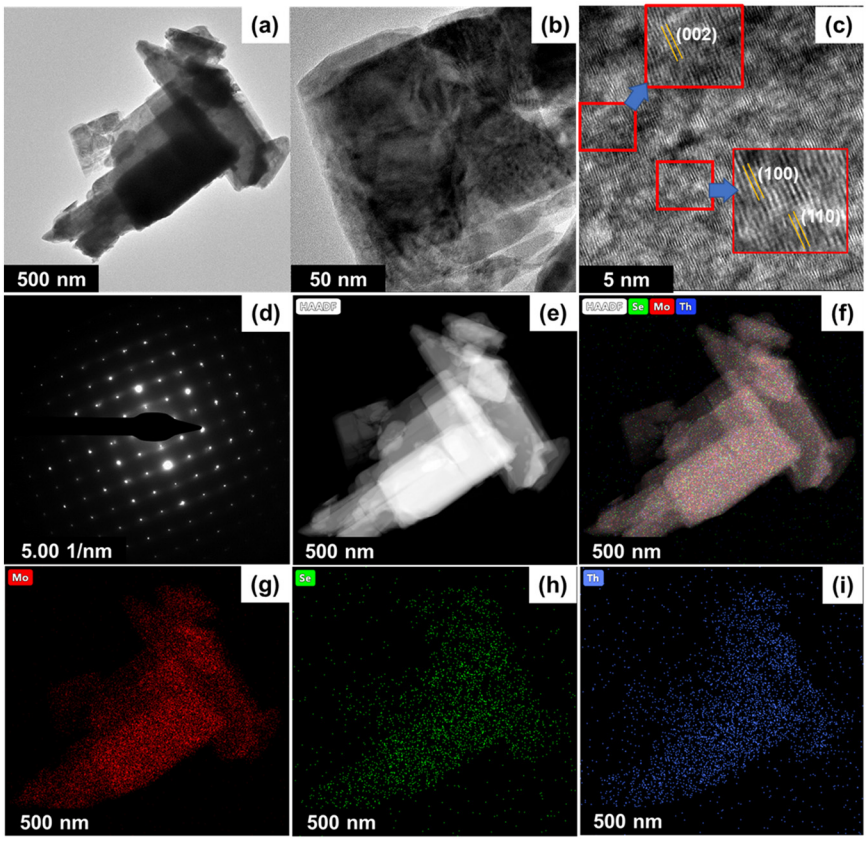

Fig. 8 (a–c) HR-TEM images of Th-doped $MoSe_2$, (c) corresponding FFT images indicated by the red boxes, (d) SAED pattern of the polycrystalline film, (e) HAADF image of Th-doped $MoSe_2$, (f) combined HAADF mapping of elements for Th-doped $MoSe_2$, and (g–i) elemental mapping of Mo, Se, and Th, respectively.

Preliminary experimental evidence of methanol oxidation on Th-doped $MoSe_2$

To assess the physical characteristics of Th-doped $MoSe_2$, nitrogen (N_2) adsorption measurements were performed, including N_2 adsorption–desorption isotherms, and pore size distribution was analysed, as shown in Fig. 9(a). The Th-doped $MoSe_2$ catalyst exhibits type-V isotherms with H1 type hysteresis loops, characteristic of non-porous to weakly mesoporous materials. Brunauer–Emmett–Teller (BET)[72] surface area analysis reveals a specific surface area of approximately 0.57 $m^2\ g^{-1}$ for the Th-doped $MoSe_2$ catalyst. Additionally, the pore size distribution, derived from desorption data using the Barrett–Joyner–Halenda (BJH) model, is shown in Fig. 9(a) (inset). The total pore volume of the Th-doped $MoSe_2$ catalyst was measured to be $\sim 9.2 \times 10^{-3}$ cc g^{-1}. The mesoporous structure significantly enhances the exposure of active sites, thereby improving the efficiency of catalytic processes, particularly in the case of the MOR. The ordered surface area of Th-doped $MoSe_2$ facilitates enhanced adsorption and diffusion of reactants, contributing to improved catalytic activity.

The interaction of the catalyst with methanol, including its adsorption and desorption behaviour, can differ across materials due to variations in composition, morphology, porosity, and surface area. These factors play a crucial role in determining the availability of methanol at catalytic sites, subsequently impacting the current density. Therefore, various electrochemical measurements were carried out as shown in Fig. 9(b–f).

The electrocatalytic efficiency of Th-doped $MoSe_2$ for the MOR was evaluated using CV of a 0.5 M H_2SO_4 + 0.5 M CH_3OH solution, as illustrated in Fig. 9(b). A distinct peak indicative of MOR activity was observed at ~1.12 V *vs.* RHE, with a current density of 0.20 mA cm^{-2} for Th-doped $MoSe_2$ at a scan rate of 10 mV s^{-1}. The CV profiles of the Th-doped $MoSe_2$ catalyst exhibit a well-defined anodic peak in both forward (I_f) and backward (I_b) scans. The forward scan reflects the extent of methanol oxidation at the electrode modified with the catalyst, while the backward scan displays hysteresis due to the oxidation of electro-generated intermediates during the forward sweep. Further analysis using LSV revealed that the onset potential for the MOR with Th-doped $MoSe_2$ is around 1.02 V *vs.* RHE (Fig. 9(c)). The Tafel slope (Fig. 9(d)), derived from the LSV curves using the Tafel equation, indicates a lower value for the MOR with Th-doped $MoSe_2$, implying a higher exchange current density at the catalyst–electrode interfaces, which is advantageous for practical applications and indicates improved MOR

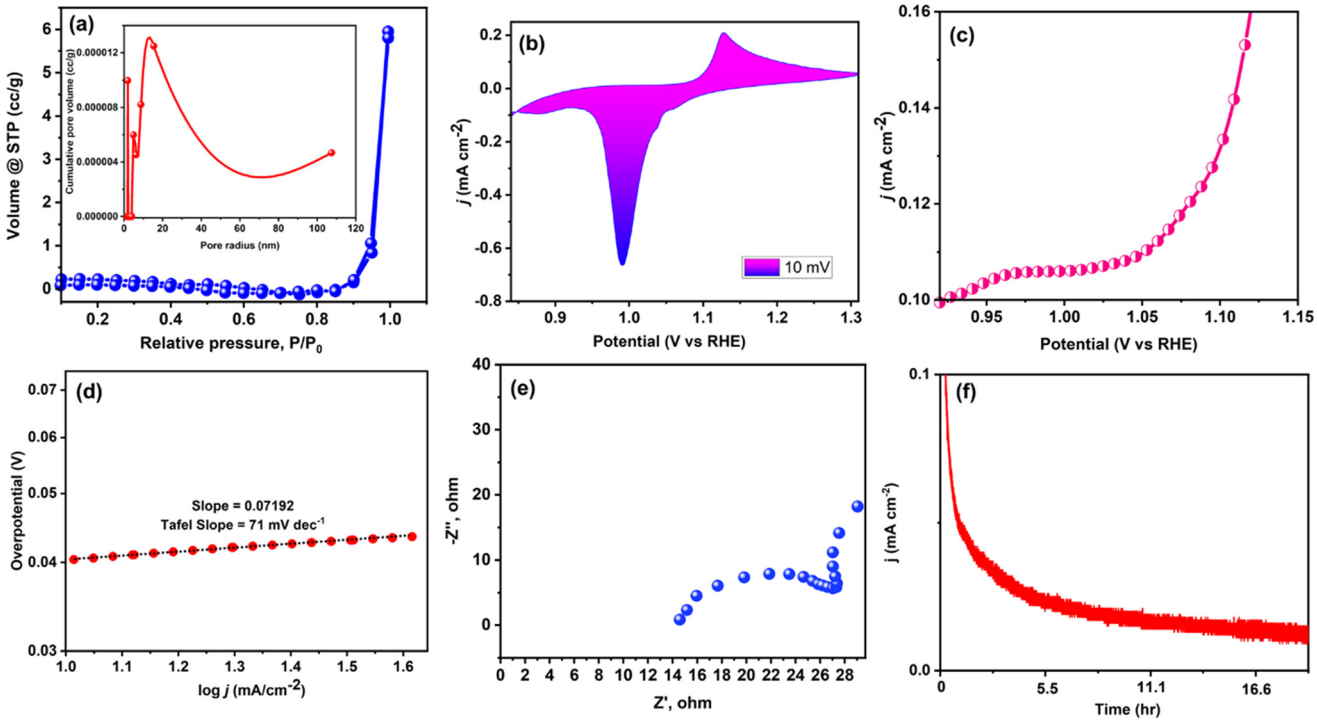

Fig. 9 (a) N_2 adsorption and desorption isotherms, along with the (inset) pore size distribution graph, (b) CV profiles of 0.5 M H_2SO_4 + 0.5 M CH_3OH solution at a scan rate of 10 mV s^{-1} *versus* RHE, (c) LSV curve of 0.5 M H_2SO_4 + 0.5 M CH_3OH solution at a scan rate of 50 mV s^{-1} *versus* RHE, (d) Tafel plot, (e) Nyquist plot, and (f) chronoamperometry (*I*–*t*) curve.

kinetics within the investigated potential range. To investigate the electroanalytical properties of Th-doped $MoSe_2$, electrochemical impedance spectroscopy (EIS) was conducted, as illustrated in Fig. 9(e). The resulting Nyquist plot reveals a semicircular arc in the lower-frequency region, providing direct evidence of the charge transfer process while offering insights into the reaction kinetics. Th-doped $MoSe_2$ exhibits the lowest charge transfer resistance (R_{ct}) of 1.98 Ω, indicating its superior electrochemical performance compared to other catalysts, as shown in the SI (Table S3). The EIS data also demonstrate that the Th-doping significantly enhances the electron transfer efficiency, making it a promising candidate for faster electro-oxidation of the MOR. The corresponding equivalent EIS fitting circuit is provided in the SI (Fig. S5(a)) to support these findings. In addition, the long-term stability of the Th-doped $MoSe_2$ catalyst for the MOR was assessed using current–time (*I*–*t*). The *I*–*t* measurements were conducted at a constant potential of 1.0 V *vs.* RHE for 20 hours, and the results are shown in Fig. 9(f). It is observed that Th-doped $MoSe_2$ is stable up to 12 hours.

The prominent reduction peak observed at around 0.9 V in the backward scan of the CV suggests that fresh active sites are regenerated upon reversal of the potential sweep. This facilitates renewed adsorption of methanol, leading to its chemisorption and subsequent oxidation, thereby producing a pronounced cathodic current. This behavior is consistent with previous reports, where the backward scan is often attributed to the removal of residual intermediates and the reactivation of the catalytic surface for fresh methanol adsorption and oxidation.[73,74]

The effect of varying scan rates on the MOR activity of Th-doped $MoSe_2$ was further studied, as shown in the SI (Fig. S5(b)). CV measurements conducted in 0.5 M H_2SO_4 + 0.5 M CH_3OH at scan rates from 10 to 100 mV s^{-1} revealed a linear increase in both anodic and cathodic current densities with higher scan rates (see the SI (Fig. S5(b))), suggesting that the MOR current density is diffusion-limited. Additionally, the linear relationship between the peak current and scan rate, highlighted within a yellow box in the SI (Fig. S5(b)), confirms the diffusion-limited nature of the electrochemical process. Durability was also tested over continuous 100 CV cycles with a scan rate of 50 mV s^{-1}, demonstrating the stability of the catalyst, as shown in the SI (Fig. S5(c)). A gradual decrease in current density was observed with increasing cycle number. This attenuation is primarily attributed to temporary surface passivation, arising from the accumulation of reaction intermediates (*e.g.*, CO and CH_xO species) that adsorb onto active sites and inhibit further methanol oxidation. Furthermore, a comparative

Table 2 Comparative electrochemical performance of Th-doped and undoped $MoSe_2$

Sample		Onset potential	Scan rate
$MoSe_2$	Th-doped	1.02 V *vs.* RHE	50 mV s^{-1}
	Undoped	2.50 V *vs.* RHE	50 mV s^{-1}

electrochemical analysis of $MoSe_2$ and Th-doped $MoSe_2$ was conducted as shown in Table 2.

Under identical experimental conditions and at a scan rate of 50 mV s^{-1}, pristine $MoSe_2$ exhibits an onset potential of 2.50 V *vs.* RHE for methanol oxidation (Fig. S5(d and e)). In contrast, Th-doped $MoSe_2$ shows a substantially reduced onset potential of 1.02 V *vs.* RHE, clearly demonstrating the enhanced catalytic activity induced by Th incorporation. The CV curve of the Th-doped $MoSe_2$ catalyst in 0.5 M H_2SO_4 is shown in the SI, Fig. S5(f).

Moreover, the calculated mass activity (M_A) of the Th-doped $MoSe_2$ catalyst is 0.400 A mg^{-1}, which is significantly higher than those of several reported Pt-based catalysts, such as Pt/gCN (0.310 A mg^{-1}),[75] Pt/NiCo-LDH (0.379 A mg^{-1}),[76] and Pt/NiCo-LDH (0.205 A mg^{-1}).[77] The detailed M_A calculation is provided in the SI. The comparison of MOR performance between the considered catalyst and other nano-catalysts is summarised in the SI (Tables S2 and S3). The low R_{ct} value and onset potential of Th-doped $MoSe_2$ demonstrate superior methanol oxidation performance compared to previously reported catalysts. The intrinsic catalytic performance of Th-doped $MoSe_2$ was evaluated by calculating the electrochemically active surface area (ECSA), and the corresponding specific activity (SA) is provided in the SI (Fig. S6(a)).

Despite its low BET surface area, the enhanced MOR performance of Th-doped $MoSe_2$ arises from Th-induced electronic structure modulation that improves charge transfer and optimizes intermediate adsorption, leading to higher intrinsic catalytic activity.

CO stripping analysis

The inactivation of Th-doped $MoSe_2$ is attributed to the poisoning of the catalyst by the reaction intermediate CO during methanol oxidation. To explore the anti-poisoning mechanism of the Th-doped $MoSe_2$ catalyst for the MOR, CO stripping analysis is performed. The curve in the SI (Fig. S6(b)) reveals the anti-CO poisoning ability of the Th-doped $MoSe_2$ catalyst. CO gas was purged into the 0.5 M H_2SO_4 electrolyte solution for 1 hour, allowing the CO molecules to adsorb onto the active sites of the electrocatalyst. Finally, N_2 gas was used again to purge the solution, eliminating any dissolved CO, and then CV was performed at a scan rate of 10 mV s^{-1}. The absence of the oxidation peak indicates that CO has been fully oxidized on the surface of Th-doped $MoSe_2$. Furthermore, experimental analysis using ^{13}C NMR (SI, Fig. S7), ^{1}H-NMR (SI, Fig. S8), and FTIR (SI, Fig. S9) spectroscopy was performed after the electro-oxidation of methanol. The ^{13}C NMR and ^{1}H-NMR analysis of the liquid electrolyte obtained after the MOR verifies the complete conversion of CH_3OH to CO_2, with no other products detected. The absence of the FTIR peak of CO after electrocatalysis supports the notion that CO is not adsorbed on the Th-doped $MoSe_2$ catalyst. The theoretical analysis shows that the ΔG of CO in Scheme 3 (ΔG = 0.45 eV) suggests very weak adsorption of CO on the catalyst surface, which enhances anti-poisoning activity by preventing CO from blocking the surface. These results collectively confirm that Scheme 3 is the most effective for the MOR on Th-doped $MoSe_2$ catalysts.

Conclusion

Th-doped $MoSe_2$ was successfully synthesized *via* a hydrothermal method and characterized as a high-performance electrocatalyst for the MOR. Structural analyses (XRD, HR-TEM, and XPS) confirmed the incorporation of Th into the $MoSe_2$ lattice, while BET measurements revealed a mesoporous morphology (0.578 m^2 g^{-1}) conducive to active-site accessibility. Electrochemically, the catalyst exhibited exceptional activity, with a low onset potential (1.02 V *vs.* RHE), high current density, and ultralow charge-transfer resistance, outperforming undoped $MoSe_2$ and many Pt-based alternatives. The mass activity of Th-doped $MoSe_2$ (0.400 A mg^{-1}) was significantly higher than those of various Pt-based catalysts, emphasizing its potential as a cost-effective and efficient alternative. DFT calculations elucidated the role of Th doping in reducing the bandgap and generating Se-centered active sites, which facilitated methanol adsorption and dehydrogenation *via* the energetically favored CHOH pathway (ΔG = −1.89 eV). The catalyst's anti-poisoning capability was validated through CO stripping experiments and spectroscopic techniques, which showed efficient CO desorption and complete methanol conversion to CO_2. This study bridges synthesis, characterization, and computational modeling to provide a holistic understanding of catalytic mechanisms of Th-doped $MoSe_2$. The material's durability (12 hour stability), cost-effectiveness, and resistance to CO poisoning position it as a viable candidate for renewable energy systems. Future research may focus on dopant engineering, heterostructure formation, or composite hybridization to further improve catalytic performance and broaden the scope of application in sustainable energy conversion technologies.

Conflicts of interest

The authors declare no competing financial interest.

Data availability

All the data supporting the findings of this article are provided in the supplementary information (SI).

Supplementary information: the detailed experimental and theoretical methodology used in the present investigation is provided in the Materials and method section, EDS, XPS, and XRD analyses, electro-oxidation of methanol, optimized geometry with the important geometrical parameter of Th-doped $MoSe_2$, differential charge density analysis, band structure, elementary steps in the MOR involving electron transfer, along with their corresponding reaction free energy expressions and their electronic properties, CO stripping analysis, ^{13}C NMR, ^{1}H-

NMR, and FTIR analyses, and comparison between the synthesised catalyst and other Pt-based nano-catalysts. See DOI: https://doi.org/10.1039/d5lf00356c.

Acknowledgements

We are thankful to funding agency DST-SERB (EEQ/2023/000424, ECR/2018/002346 and EEQ/2019/000656) Delhi, India for providing financial support. We are also thankful to the Director, National Institute of Technology Warangal for providing the facilities. One of the authors, Pooja, is also thankful to the Ministry of Education (MoE), formerly the Ministry of Human Resource Development (MHRD), for providing a Senior Research Fellowship (SRF). We would also like to thank IIT Kanpur for providing the XPS facility, IIT-ISM Dhanbad for the HRTEM facility, and NIT Warangal for the FESEM and XRD facilities.

References

1 C. Liu and L. Feng, Advances in Anode Catalysts of Methanol-Assisted Water-Splitting Reactions for Hydrogen Generation, *Chin. J. Struct. Chem.*, 2023, **42**(10), 100136, DOI: 10.1016/j.cjsc.2023.100136.

2 X. Duan, T. Li, X. Jiang, X. Liu, L. Xin, H. Yang, Y. Kuang and X. Sun, Catalytic Applications of Single-Atom Metal-Anchored Hydroxides: Recent Advances and Perspective, *Mater. Rep.: Energy*, 2022, **2**(3), 100146, DOI: 10.1016/j.matre.2022.100146.

3 Y. Zhou, Q. Wang, X. Tian, J. Chang and L. Feng, Electron-Enriched Pt Induced by $CoSe_2$ Promoted Bifunctional Catalytic Ability for Low Carbon Alcohol Fuel Electro-Reforming of Hydrogen Evolution, *J. Energy Chem.*, 2022, **75**, 46–54, DOI: 10.1016/j.jechem.2022.08.009.

4 X. Sun, Y.-J. Song, R.-L. Li and J.-J. Wang, Catalytic Effect of Disordered Ru-O Configurations for Electrochemical Hydrogen Evolution. *Journal of*, *Electrochemistry*, 2022, **28**(10), 2214011, DOI: 10.13208/j.electrochem.2214011.

5 W. Qiao, X. Huang and L. Feng, Advances of PtRu-Based Electrocatalysts for Methanol Oxidation, *Chin. J. Struct. Chem.*, 2022, **41**(7), 2207016–2207034, DOI: 10.14102/j.cnki.0254-5861.2022-0098.

6 F. Guo, T. J. Macdonald, A. J. Sobrido, L. Liu, J. Feng and G. He, Recent Advances in Ultralow-Pt-Loading Electrocatalysts for the Efficient Hydrogen Evolution, *Adv. Sci.*, 2023, **10**(21), 2301098, DOI: 10.1002/advs.202301098.

7 A. R. Poerwoprajitno, L. Gloag, J. Watt, S. Cheong, X. Tan, H. Lei, H. A. Tahini, A. Henson, B. Subhash, N. M. Bedford, B. K. Miller, P. B. O'Mara, T. M. Benedetti, D. L. Huber, W. Zhang, S. C. Smith, J. J. Gooding, W. Schuhmann and R. D. Tilley, A Single-Pt-Atom-on-Ru-Nanoparticle Electrocatalyst for CO-Resilient Methanol Oxidation, *Nat. Catal.*, 2022, **5**(3), 231–237, DOI: 10.1038/s41929-022-00756-9.

8 N. S. Sapienza, K. N. Knight, M. Albrahim, M. R. Yousuf, A. M. Karim and J. R. Morris, Autocatalysis through the Generation of Water during Methanol Oxidation over a Titania-Supported Platinum Catalyst, *ACS Catal.*, 2023, **13**(15), 9997–10006, DOI: 10.1021/acscatal.3c01740.

9 J. Greeley, T. F. Jaramillo, J. Bonde, I. Chorkendorff and J. K. Nørskov, Computational High-Throughput Screening of Electrocatalytic Materials for Hydrogen Evolution, *Nat. Mater.*, 2006, **5**(11), 909–913, DOI: 10.1038/nmat1752.

10 D. Vikraman, K. Akbar, S. Hussain, G. Yoo, J.-Y. Jang, S.-H. Chun, J. Jung and H. J. Park, Direct Synthesis of Thickness-Tunable MoS_2 Quantum Dot Thin Layers: Optical, Structural and Electrical Properties and Their Application to Hydrogen Evolution, *Nano Energy*, 2017, **35**, 101–114, DOI: 10.1016/j.nanoen.2017.03.031.

11 X. Zhou, Y. Liu, H. Ju, B. Pan, J. Zhu, T. Ding, C. Wang and Q. Yang, Design and Epitaxial Growth of $MoSe_2$–NiSe Vertical Heteronanostructures with Electronic Modulation for Enhanced Hydrogen Evolution Reaction, *Chem. Mater.*, 2016, **28**(6), 1838–1846, DOI: 10.1021/acs.chemmater.5b05006.

12 D. Gao, B. Xia, Y. Wang, W. Xiao, P. Xi, D. Xue and J. Ding, Dual-Native Vacancy Activated Basal Plane and Conductivity of $MoSe_2$ with High-Efficiency Hydrogen Evolution Reaction, *Small*, 2018, **14**(14), 1704150, DOI: 10.1002/smll.201704150.

13 Y. Kuang, W. Qiao, S. Wang, F. Yang and L. Feng, Doping and Interfacial Engineering of $MoSe_2$ Nanosheets by NH_3 Plasma Promoted Pt for Methanol Electrolysis, *ACS Mater. Lett.*, 2024, **6**(5), 1722–1731, DOI: 10.1021/acsmaterialslett.4c00244.

14 A. Eftekhari, Molybdenum Diselenide ($MoSe_2$) for Energy Storage, Catalysis, and Optoelectronics, *Appl. Mater. Today*, 2017, **8**, 1–17, DOI: 10.1016/j.apmt.2017.01.006.

15 M. B. Wazir, M. Daud, S. Safeer, F. Almarzooqi and A. Qurashi, Review on 2D Molybdenum Diselenide ($MoSe_2$) and Its Hybrids for Green Hydrogen (H_2) Generation Applications, *ACS Omega*, 2022, **7**(20), 16856–16865, DOI: 10.1021/acsomega.2c00330.

16 X. Xia, L. Wang, N. Sui, V. L. Colvin and W. W. Yu, Recent Progress in Transition Metal Selenide Electrocatalysts for Water Splitting, *Nanoscale*, 2020, **12**(23), 12249–12262, DOI: 10.1039/D0NR02939D.

17 D. Kong, H. Wang, J. J. Cha, M. Pasta, K. J. Koski, J. Yao and Y. Cui, Synthesis of MoS_2 and $MoSe_2$ Films with Vertically Aligned Layers, *Nano Lett.*, 2013, **13**(3), 1341–1347, DOI: 10.1021/nl400258t.

18 H. Liu, H. Guo, B. Liu, M. Liang, Z. Lv, K. R. Adair and X. Sun, Few-Layer $MoSe_2$ Nanosheets with Expanded (002) Planes Confined in Hollow Carbon Nanospheres for Ultrahigh-Performance Na-Ion Batteries, *Adv. Funct. Mater.*, 2018, **28**(19), 1707480, DOI: 10.1002/adfm.201707480.

19 J. Kibsgaard, Z. Chen, B. N. Reinecke and T. F. Jaramillo, Engineering the Surface Structure of MoS_2 to Preferentially Expose Active Edge Sites for Electrocatalysis, *Nat. Mater.*, 2012, **11**(11), 963–969, DOI: 10.1038/nmat3439.

20 Y. Liu, G. Jiang, Z. Huang, Q. Lu, B. Yu, U. Evariste and P. Ma, Decoration of Hollow Mesoporous Carbon Spheres by $NiCo_2S_4$ Nanoparticles as Electrode Materials for Asymmetric

Supercapacitors, *ACS Appl. Energy Mater.*, 2019, **2**(11), 8079–8089, DOI: 10.1021/acsaem.9b01569.

21 J. Li, C. Tang, H. Zhang, Z. Zou and C. M. Li, Mesoporous Molybdenum Carbide for Greatly Enhanced Hydrogen Evolution at High Current Density and Its Mechanism Studies, *Mater. Rep.: Energy*, 2023, **3**(3), 100215, DOI: 10.1016/j.matre.2023.100215.

22 C. Zhang, J. Li, C. Li, W. Chen and C. Guo, Surface and Interface Engineering of Hollow Carbon Sphere-Based Electrocatalysts for the Oxygen Reduction Reaction, *J. Mater. Chem. A*, 2021, **9**(46), 25706–25730, DOI: 10.1039/D1TA06913F.

23 W. Chen, R. Qiao, C. Song, L. Zhao, Z.-J. Jiang, T. Maiyalagan and Z. Jiang, Tailoring the Thickness of $MoSe_2$ Layer of the Hierarchical Double-Shelled N-Doped carbon@$MoSe_2$ Hollow Nanoboxes for Efficient and Stable Hydrogen Evolution Reaction, *J. Catal.*, 2020, **381**, 363–373, DOI: 10.1016/j.jcat.2019.11.013.

24 S. Pan, Z. Cai, L. Yang, B. Tang, X. Xu, H. Chen, L. Ran, B. Jing and J. Zou, Exposure of Sufficient Edge Sites on Well-Crystallized $MoSe_2$ Induced by Nitrogen Doping (Mo–Nx) for Pt: Enhanced Co-Catalytic Activity and Methanol Tolerance for Oxygen Reduction, *Energy*, 2018, **159**, 11–20, DOI: 10.1016/j.energy.2018.06.114.

25 J. Ruan, Y. Chen, G. Zhao, P. Li, B. Zhang, Y. Jiang, T. Ma, H. Pan, S. X. Dou and W. Sun, Cobalt Single Atoms Enabling Efficient Methanol Oxidation Reaction on Platinum Anchored on Nitrogen-Doped Carbon, *Small*, 2022, **18**(43), 2107067, DOI: 10.1002/smll.202107067.

26 X. Ren, Q. Ma, P. Ren and Y. Wang, Synthesis of Nitrogen-Doped $MoSe_2$ Nanosheets with Enhanced Electrocatalytic Activity for Hydrogen Evolution Reaction, *Int. J. Hydrogen Energy*, 2018, **43**(32), 15275–15280, DOI: 10.1016/j.ijhydene.2018.06.122.

27 A. Shafqat, T. Iqbal and A. Majid, A DFT Study of Intrinsic Point Defects in Monolayer $MoSe_2$, *AIP Adv.*, 2017, **7**(10), 105306, DOI: 10.1063/1.4999524.

28 H. Shu, D. Zhou, F. Li, D. Cao and X. Chen, Defect Engineering in $MoSe_2$ for the Hydrogen Evolution Reaction: From Point Defects to Edges, *ACS Appl. Mater. Interfaces*, 2017, **9**(49), 42688–42698, DOI: 10.1021/acsami.7b12478.

29 H.-P. Komsa and A. V. Krasheninnikov, Native Defects in Bulk and Monolayer ${\mathrm{MoS}}_{2}$ from First Principles, *Phys. Rev. B: Condens. Matter Mater. Phys.*, 2015, **91**(12), 125304, DOI: 10.1103/PhysRevB.91.125304.

30 L. Lin, N. Miao, Y. Wen, S. Zhang, P. Ghosez, Z. Sun and D. A. Allwood, Sulfur-Depleted Monolayered Molybdenum Disulfide Nanocrystals for Superelectrochemical Hydrogen Evolution Reaction, *ACS Nano*, 2016, **10**(9), 8929–8937, DOI: 10.1021/acsnano.6b04904.

31 A. A. Tedstone, D. J. Lewis and P. O'Brien, Synthesis, Properties, and Applications of Transition Metal-Doped Layered Transition Metal Dichalcogenides, *Chem. Mater.*, 2016, **28**(7), 1965–1974, DOI: 10.1021/acs.chemmater.6b00430.

32 X. Chen, Y. Qiu, G. Liu, W. Zheng, W. Feng, F. Gao, W. Cao, Y. Fu, W. Hu and P. Hu, Tuning Electrochemical Catalytic Activity of Defective 2D Terrace $MoSe_a$ Heterogeneous Catalyst via Cobalt Doping, *J. Mater. Chem. A*, 2017, **5**(22), 11357–11363, DOI: 10.1039/C7TA02327H.

33 C. Xu, S. Peng, C. Tan, H. Ang, H. Tan, H. Zhang and Q. Yan, Ultrathin S-Doped $MoSe_2$ Nanosheets for Efficient Hydrogen Evolution, *J. Mater. Chem. A*, 2014, **2**(16), 5597–5601, DOI: 10.1039/C4TA00458B.

34 Q. Niu, T.-Y. Yu, J.-W. Shi, Q. Huang, L.-Z. Dong, F. Yu, S.-L. Li, J. Liu and Y.-Q. Lan, Constructing Functional Radiation-Resistant Thorium Clusters for Catalytic Redox Reactions, *J. Am. Chem. Soc.*, 2024, **146**(30), 20649–20659, DOI: 10.1021/jacs.4c03126.

35 Y. Xue, D. Pan, F. Zuo, S. Xiao, X. Li, F. Lou, M. Li and Y. Ouyang, Improved Performance of Self-Reactivated Pt–ThO_2/C Catalysts in a Direct Ethanol Fuel Cell, *RSC Adv.*, 2022, **12**(27), 17012–17019, DOI: 10.1039/D2RA02398A.

36 K. C. Park, J. Lim, G. C. Thaggard and N. B. Shustova, Mining for Metal–Organic Systems: Chemistry Frontiers of Th-, U-, and Zr-Materials, *J. Am. Chem. Soc.*, 2024, **146**(27), 18189–18204, DOI: 10.1021/jacs.4c06088.

37 Z.-J. Li, X. Guo, J. Qiu, H. Lu, J.-Q. Wang and J. Lin, Recent Advances in the Applications of Thorium-Based Metal–Organic Frameworks and Molecular Clusters, *Dalton Trans.*, 2022, **51**(19), 7376–7389, DOI: 10.1039/D2DT00265E.

38 D. Das, R. Gupta, S. K. Gupta, A. K. Yadav and K. Sudarshan, Tailoring Oxygen Vacancies in ThO_2 for Improved Light Emission and ORR Electrocatalysis, *Mater. Today Chem.*, 2023, **32**, 101635, DOI: 10.1016/j.mtchem.2023.101635.

39 Z.-J. Li, Z. Yue, Y. Ju, X. Wu, Y. Ren, S. Wang, Y. Li, Z.-H. Zhang, X. Guo, J. Lin and J.-Q. Wang, Ultrastable Thorium Metal–Organic Frameworks for Efficient Iodine Adsorption, *Inorg. Chem.*, 2020, **59**(7), 4435–4442, DOI: 10.1021/acs.inorgchem.9b03602.

40 S. Hou, F. Liu, H. Xie, S. L. Hanna, K. B. Idrees, C. Zhang, X. Wang, Y. Chen, P. Li and O. K. Farha, Unveiling the Structure–Modulator Relationships in Thorium-Based Metal–Organic Framework Crystallization, *Inorg. Chem.*, 2023, **62**(14), 5479–5486, DOI: 10.1021/acs.inorgchem.2c04447.

41 Z. Sofer, O. Jankovský, P. Šimek, K. Klímová, A. Macková and M. Pumera, Uranium- and Thorium-Doped Graphene for Efficient Oxygen and Hydrogen Peroxide Reduction, *ACS Nano*, 2014, **8**(7), 7106–7114, DOI: 10.1021/nn502026k.

42 S. K. Gupta, M. K. Bhide, S. V. Godbole and V. Natarajan, Probing Site Symmetry Around Eu^{3+} in Nanocrystalline ThO_2 Using Time Resolved Emission Spectroscopy, *J. Am. Ceram. Soc.*, 2014, **97**(11), 3694–3701, DOI: 10.1111/jace.13143.

43 J. Hafner and G. Kresse, The Vienna AB-Initio Simulation Program VASP: An Efficient and Versatile Tool for Studying the Structural, Dynamic, and Electronic Properties of Materials, in *Properties of Complex Inorganic Solids*, ed. A. Gonis, A. Meike and P. E. A. Turchi, Springer US, Boston, MA, 1997, pp. 69–82, DOI: 10.1007/978-1-4615-5943-6_10.

44 G. Sun, J. Kürti, P. Rajczy, M. Kertesz, J. Hafner and G. Kresse, Performance of the Vienna Ab Initio Simulation Package (VASP) in Chemical Applications, *J. Mol. Struct.: THEOCHEM*, 2003, **624**(1), 37–45, DOI: 10.1016/S0166-1280(02)00733-9.

45 M. Topsakal and R. M. Wentzcovitch, Accurate Projected Augmented Wave (PAW) Datasets for Rare-Earth Elements (RE = La–Lu), *Comput. Mater. Sci.*, 2014, **95**, 263–270, DOI: 10.1016/j.commatsci.2014.07.030.

46 L. He, F. Liu, G. Hautier, M. J. T. Oliveira, M. A. L. Marques, F. D. Vila, J. J. Rehr, G.-M. Rignanese and A. Zhou, Accuracy of Generalized Gradient Approximation Functionals for Density-Functional Perturbation Theory Calculations, *Phys. Rev. B: Condens. Matter Mater. Phys.*, 2014, **89**(6), 064305, DOI: 10.1103/PhysRevB.89.064305.

47 J. P. Perdew and W. Yue, Accurate and Simple Density Functional for the Electronic Exchange Energy: Generalized Gradient Approximation, *Phys. Rev. B: Condens. Matter Mater. Phys.*, 1986, **33**(12), 8800–8802, DOI: 10.1103/PhysRevB.33.8800.

48 H. J. Monkhorst and J. D. Pack, Special Points for Brillouin-Zone Integrations, *Phys. Rev. B*, 1976, **13**(12), 5188–5192, DOI: 10.1103/PhysRevB.13.5188.

49 J. K. Nørskov, J. Rossmeisl, A. Logadottir, L. Lindqvist, J. R. Kitchin, T. Bligaard and H. Jónsson, Origin of the Overpotential for Oxygen Reduction at a Fuel-Cell Cathode, *J. Phys. Chem. B*, 2004, **108**(46), 17886–17892, DOI: 10.1021/jp047349j.

50 L. Pecher and R. Tonner, Deriving Bonding Concepts for Molecules, Surfaces, and Solids with Energy Decomposition Analysis for Extended Systems, *WIREs Comput. Mol. Sci.*, 2019, **9**(4), e1401, DOI: 10.1002/wcms.1401.

51 G. te Velde and E. J. Baerends, Precise Density-Functional Method for Periodic Structures, *Phys. Rev. B: Condens. Matter Mater. Phys.*, 1991, **44**(15), 7888–7903, DOI: 10.1103/PhysRevB.44.7888.

52 G. te Velde, F. M. Bickelhaupt, E. J. Baerends, C. Fonseca Guerra, S. J. A. van Gisbergen, J. G. Snijders and T. Ziegler, Chemistry with ADF, *J. Comput. Chem.*, 2001, **22**(9), 931–967, DOI: 10.1002/jcc.1056.

53 R. S. Mulliken, Self-Consistent Field Atomic and Molecular Orbitals and Their Approximations as Linear Combinations of Slater-Type Orbitals, *Rev. Mod. Phys.*, 1960, **32**(2), 232–238, DOI: 10.1103/RevModPhys.32.232.

54 B. Hammer, K. W. Jacobsen and J. K. Nørskov, Role of Nonlocal Exchange Correlation in Activated Adsorption, *Phys. Rev. Lett.*, 1993, **70**(25), 3971–3974, DOI: 10.1103/PhysRevLett.70.3971.

55 M. Andersen, Revelations of the d Band, *Nat. Catal.*, 2023, **6**(6), 460–461, DOI: 10.1038/s41929-023-00964-x.

56 K. Li, Z. Tao, X. Ma, J. Wu, T. Wu, C. Guo, Y. Qi, J. Yu, J. Zheng and J. Xue, The Application and Research Progress of D-Band Center Theory in the Field of Water Electrolysis, *Int. J. Hydrogen Energy*, 2025, **132**, 183–211, DOI: 10.1016/j.ijhydene.2025.02.305.

57 J. K. Nørskov, T. Bligaard, J. Rossmeisl and C. H. Christensen, Towards the Computational Design of Solid Catalysts, *Nat. Chem.*, 2009, **1**(1), 37–46, DOI: 10.1038/nchem.121.

58 S. Bhattacharjee, U. V. Waghmare and S.-C. Lee, An Improved D-Band Model of the Catalytic Activity of Magnetic Transition Metal Surfaces, *Sci. Rep.*, 2016, **6**, 35916, DOI: 10.1038/srep35916.

59 J. K. Nørskov, F. Abild-Pedersen, F. Studt and T. Bligaard, Density Functional Theory in Surface Chemistry and Catalysis, *Proc. Natl. Acad. Sci. U. S. A.*, 2011, **108**(3), 937–943, DOI: 10.1073/pnas.1006652108.

60 K. Vasu, O. E. Meiron, A. N. Enyashin, R. Bar-Ziv and M. Bar-Sadan, Effect of Ru Doping on the Properties of $MoSe_2$ Nanoflowers, *J. Phys. Chem. C*, 2019, **123**(3), 1987–1994, DOI: 10.1021/acs.jpcc.8b11712.

61 F. Zhong, J. Ye, T. He, L. Zhang, Z. Wang, Q. Li, B. Han, P. Wang, P. Wu, Y. Yu, J. Guo, Z. Zhang, M. Peng, T. Xu, X. Ge, Y. Wang, H. Wang, M. Zubair, X. Zhou, P. Gao, Z. Fan and W. Hu, Substitutionally Doped $MoSe_2$ for High-Performance Electronics and Optoelectronics, *Small*, 2021, **17**(47), 2102855, DOI: 10.1002/smll.202102855.

62 D. Shen, B. Zhao, Z. Zhang, H. Zhang, X. Yang, Z. Huang, B. Li, R. Song, Y. Jin, R. Wu, B. Li, J. Li and X. Duan, Synthesis of Group VIII Magnetic Transition-Metal-Doped Monolayer $MoSe_2$, *ACS Nano*, 2022, **16**(7), 10623–10631, DOI: 10.1021/acsnano.2c02214.

63 J. Zhang, Y. Xia, Z. Yu, X. Yue, Y. Jin, M. Yuan, Y. Feng, B. Li, B. Wang, W. Ho, C. Liu, H. Xu, C. Jin and M. Xie, Niobium and Rhenium Doping in $MoSe_2$ Monolayer during Molecular Beam Epitaxy: Shallow Dopants and Defect Proliferation, *APL Mater.*, 2023, **11**(7), 071113, DOI: 10.1063/5.0152247.

64 S. Y. Choi, Y. Kim, H.-S. Chung, A. R. Kim, J.-D. Kwon, J. Park, Y. L. Kim, S.-H. Kwon, M. G. Hahm and B. Cho, Effect of Nb Doping on Chemical Sensing Performance of Two-Dimensional Layered $MoSe_2$, *ACS Appl. Mater. Interfaces*, 2017, **9**(4), 3817–3823, DOI: 10.1021/acsami.6b14551.

65 D. Nam, J.-U. Lee and H. Cheong, Excitation Energy Dependent Raman Spectrum of $MoSe_2$, *Sci. Rep.*, 2015, **5**(1), 17113, DOI: 10.1038/srep17113.

66 T. Sekine, M. Izumi, T. Nakashizu, K. Uchinokura and E. Matsuura, Raman Scattering and Infrared Reflectance in 2H-$MoSe_2$, *J. Phys. Soc. Jpn.*, 1980, **49**(3), 1069–1077, DOI: 10.1143/JPSJ.49.1069.

67 X. Li, M.-W. Lin, L. Basile, S. M. Hus, A. A. Puretzky, J. Lee, Y.-C. Kuo, L.-Y. Chang, K. Wang, J. C. Idrobo, A.-P. Li, C.-H. Chen, C. M. Rouleau, D. B. Geohegan and K. Xiao, Isoelectronic Tungsten Doping in Monolayer $MoSe_2$ for Carrier Type Modulation, *Adv. Mater.*, 2016, **28**(37), 8240–8247, DOI: 10.1002/adma.201601991.

68 Y.-C. Lin, W. Zhang, J.-K. Huang, K.-K. Liu, Y.-H. Lee, C.-T. Liang, C.-W. Chu and L.-J. Li, Wafer-Scale MoS_2 Thin Layers Prepared by MoO_3 Sulfurization, *Nanoscale*, 2012, **4**(20), 6637–6641, DOI: 10.1039/C2NR31833D.

69 Y. Ding, Y. Wang, J. Ni, L. Shi, S. Shi and W. Tang, First Principles Study of Structural, Vibrational and Electronic Properties of Graphene-like MX_2 (M=Mo, Nb, W, Ta; X=S, Se,

Te) Monolayers, *Phys. B*, 2011, **406**(11), 2254–2260, DOI: 10.1016/j.physb.2011.03.044.

70 A. J. Bradley, M. M. Ugeda, F. H. da Jornada, D. Y. Qiu, W. Ruan, Y. Zhang, S. Wickenburg, A. Riss, J. Lu, S.-K. Mo, Z. Hussain, Z.-X. Shen, S. G. Louie and M. F. Crommie, Probing the Role of Interlayer Coupling and Coulomb Interactions on Electronic Structure in Few-Layer $MoSe_2$ Nanostructures, *Nano Lett.*, 2015, **15**(4), 2594–2599, DOI: 10.1021/acs.nanolett.5b00160.

71 M. Jiang, J. Zhang, M. Wu, W. Jian, H. Xue, T.-W. Ng, C.-S. Lee and J. Xu, Synthesis of 1T-$MoSe_2$ Ultrathin Nanosheets with an Expanded Interlayer Spacing of 1.17 Nm for Efficient Hydrogen Evolution Reaction, *J. Mater. Chem. A*, 2016, **4**(39), 14949–14953, DOI: 10.1039/C6TA07020E.

72 M. Naderi, Chapter Fourteen - Surface Area: Brunauer–Emmett–Teller (BET), in *Progress in Filtration and Separation*, ed. S. Tarleton, Academic Press: Oxford, 2015, pp. 585–608, DOI: 10.1016/B978-0-12-384746-1.00014-8.

73 L. Lai, G. Yang, Q. Zhang, H. Yu and F. Peng, Essential Analysis of Cyclic Voltammetry of Methanol Electrooxidation Using the Differential Electrochemical Mass Spectrometry, *J. Power Sources*, 2021, **509**, 230397, DOI: 10.1016/j.jpowsour.2021.230397.

74 D. Y. Chung, K.-J. Lee and Y.-E. Sung, Methanol Electro-Oxidation on the Pt Surface: Revisiting the Cyclic Voltammetry Interpretation, *J. Phys. Chem. C*, 2016, **120**(17), 9028–9035, DOI: 10.1021/acs.jpcc.5b12303.

75 M. Sadhukhan, M. K. Kundu, T. Bhowmik and S. Barman, Highly Dispersed Platinum Nanoparticles on Graphitic Carbon Nitride: A Highly Active and Durable Electrocatalyst for Oxidation of Methanol, Formic Acid and Formaldehyde, *Int. J. Hydrogen Energy*, 2017, **42**(15), 9371–9383, DOI: 10.1016/j.ijhydene.2017.03.097.

76 F. Zhang, Z. Wang, K. Q. Xu, J. Xia, Q. Liu and Z. Wang, Highly Dispersed Ultrafine Pt Nanoparticles on Nickel-Cobalt Layered Double Hydroxide Nanoarray for Enhanced Electrocatalytic Methanol Oxidation, *Int. J. Hydrogen Energy*, 2018, **43**(33), 16302–16310, DOI: 10.1016/j.ijhydene.2018.07.059.

77 H. Wang, Y. Chen, W. Xie, X. Han, Q. Feng, R. Jiang, H. Shang, F. Zhang, L. Gao and Z. Wang, Construction of Highly Active Pt/Ni-Fe Layered Double Hydroxide Electrocatalyst towards Methanol Oxidation in Alkaline Medium, *Int. J. Electrochem. Sci.*, 2019, **14**(8), 7961–7972, DOI: 10.20964/2019.08.06.